Numerical analysis for co-condensation processes in silicide nanoparticle synthesis using induction thermal plasmas at atmospheric pressure conditions

Masaya Shigeta[a)] and Takayuki Watanabe
Department of Environmental Chemistry and Engineering, Tokyo Institute of Technology, Midori-ku, Yokohama, 226-8503, Japan

Numerical analysis is conducted to clarify the formation mechanisms of silicide nanoparticles synthesized in an induction thermal plasma maintained at atmospheric pressure. The induction thermal plasma is analyzed by an electromagnetic fluid dynamics approach, in addition to a multi-component co-condensation model, proposed for the silicide nanoparticle synthesis. In the Cr–Si and Co–Si systems, silicon vapor is consumed by homogeneous nucleation and heterogeneous condensation processes; subsequently, metal vapor condenses heterogeneously onto liquid silicon particles. The Mo–Si system shows the opposite tendency. In the Ti–Si system, vapors of silicon and titanium condense simultaneously on the silicon nuclei. Each system produces nanoparticle diameters of around 10 nm, and the required disilicides, with the stoichiometric composition, are obtained. Only the Ti–Si system has a narrow range of silicon content. The numerical analysis results agree with the experimental findings. Finally, the correlation chart, predicting the saturation vapor pressure ratios and the resulting silicon contents, is presented for estimation of nanoparticle compositions produced in the co-condensation processes.

I. INTRODUCTION

Induction thermal plasmas (ITPs) have been widely utilized for some decades for material and environmental processes, such as nanoparticle synthesis, reactive plasma spraying, surface treatment, waste treatment, and decomposition of harmful substances.[1–4] Indeed, induction thermal plasmas have several advantages for these purposes, such as high enthalpies, high chemical reactivities, variable properties, large plasma volumes, and long residence/reaction times due to the comparatively low plasma velocities. Furthermore, induction thermal plasmas are inherently unpolluted because they are generated without the use of internal electrodes.[5,6]

The synthesis of metallic and ceramic nanoparticles of high purity can be readily achieved through the use of high quenching rates present in the tails of induction thermal plasmas.[7–9] Disilicide nanoparticles, in particular, can provide raw materials of high electrical conductivity and heat/oxidation resistance. Nanoparticles of disilicides are, therefore, expected to be interesting for application to electromagnetic shielding, solar control windows, and very large scale integration (VLSI) electrodes.

Induction thermal plasmas (ITPs) are considered to be very useful for the synthesis of silicide nanoparticles with a wide range of large vapor pressures. Furthermore, mass production of silicide nanoparticles is expected to be eventually achieved using induction thermal plasmas operated at atmospheric pressure. The actual synthesis process is, however, a complicated phenomenon involving many variables, including co-condensation processes at a range of vapor pressures. Unfortunately, only a few studies and researches have been conducted to date on the synthesis of silicide nanoparticles, using the ITPs method, to the present,[10,11] with the consequence that the formation mechanisms of these silicide nanoparticles under ITP conditions are still poorly understood. Therefore, investigations on the formation mechanisms of silicide nanoparticles are considered to be both intensively important and necessary for the precise control of particle size distributions and the corresponding stoichiometric compositions.

In the present study, numerical analysis is applied to the synthesis of silicide nanoparticles, undertaken in an induction thermal plasma. The profile of the induction thermal plasma, as used in the nanoparticle synthesis system, is initially determined by the electromagnetic fluid dynamics approach.[12] Furthermore, the state of chemical non-equilibrium of the plasma species is taken into account to estimate the more accurate transport

---

properties that directly influence the thermofluid fields and electromagnetic fields of the plasma. The obtained plasma profile is applied in the computation of silicide nanoparticle synthesis. Although some studies on nanoparticle synthesis using induction thermal plasmas have been numerically investigated by the Moment-type approach,[7,13,14] the results obtained from this approach usually have only low spatial resolution. For severe processes, in which multi-component vapors co-condense and convert to particles in very short time scales, the numerical approach, with its higher spatial resolutions, is considered to be singularly effective for investigating the mechanism of nanoparticle formation with greater accuracy. In addition, although numerical analysis was performed for the silicide nanoparticle synthesis, using ITPs, this study simply estimated the nucleation rates and nucleation temperatures only, without any consideration of the associated condensation processes.[11]

Therefore, in the present study, a multi-component co-condensation model is proposed and numerical analysis is conducted, using high spatial resolutions to clarify the mechanism of silicide nanoparticle formation, with particular reference to the chromium–silicon, cobalt–silicon, molybdenum–silicon, and titanium–silicon systems.

II. NUMERICAL MODELS

Figure 1 shows a schematic illustration of the nanoparticle synthesis system, consisting of a plasma torch
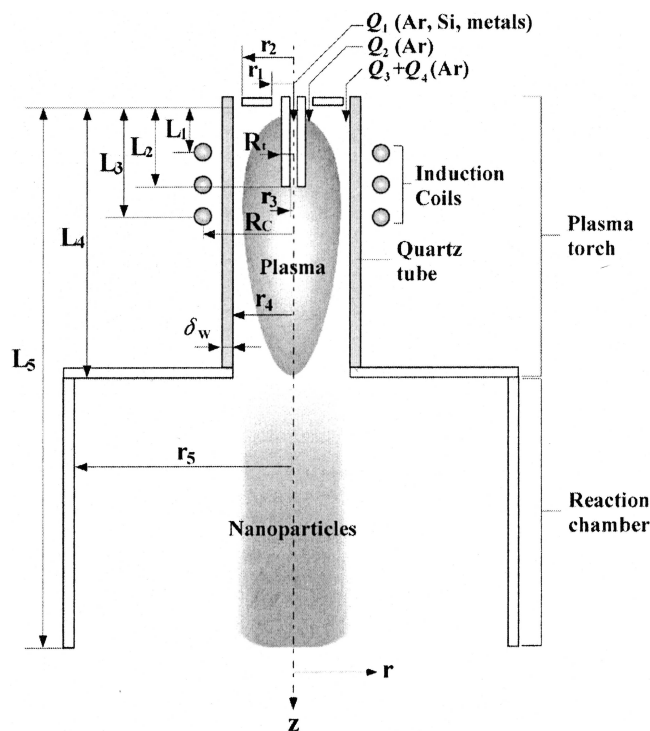

FIG. 1. Schematic illustration of nanoparticle synthesis systems.

TABLE I. Geometry and operating conditions of silicide nanoparticle synthesis systems.

Outer radius of inner slot (r_1)	6.5 mm
Outer radius of outer slot (r_2)	21.0 mm
Inner radius of injection tube (r_3)	1.0 mm
Inner radius of torch (r_4)	22.5 mm
Inner radius of torch (r_5)	100.0 mm
Outer radius of injection tube (R_t)	4.5 mm
Radius of coils (R_C)	32.0 mm
Distance to frontal end of coil (L_1)	19.0 mm
Insertion length of probe (L_2)	45.0 mm
Distance to rear end of coil (L_3)	65.0 mm
Torch length (L_3)	190.0 mm
Distance to end of chamber (L_5)	380.0 mm
Torch power	5.0 kW
Work frequency	4.0 MHz
Coil turn number	3
Pressure	101.3 kPa
Wall thickness (δ_W)	1.5 mm
Flow rate of career gas (Q_1)	1.0 Sl/min
Flow rate of plasma gas (Q_2)	3.0 Sl/min
Flow rate of plasma gas (Q_3)	10.0 Sl/min
Flow rate of sheath gas (Q_4)	20.0 Sl/min
Powder feed rate	0.1 g/min
Silicon content of feed powders	66.7 at.%

and an attached reaction chamber. A summary of the system geometry and its operating conditions is set out in Table I. The plasma torch consists of a water-cooled quartz tube, surrounded by a water-cooled induction coil. The coil, consisting of only three turns, couples its electromagnetic (EM) energy to the plasma at a frequency of 4.0 MHz. The actual delivered power level was assumed to be 5.0 kW. Argon gas is introduced as the carrier gas (1 Sl/min), the plasma supporting gas (13 Sl/min), and the sheath gas (20 Sl/min). The sheath gas, injected with an induced swirling motion from the outer slots, protects the inner surface of the quartz tube. Powders of silicon and metals are supplied (0.1 g/min) as the precursors for silicide synthesis along with the carrier gas from the central nozzle. The supplied powders are assumed to be vaporized completely due to the very high enthalpy of the thermal plasma.[11] Vapors of the injected silicon and metals are transported with the plasma flow to the reaction chamber; there they become supersaturated due to the rapid temperature decrease, which leads to homogeneous nucleation. Following the nucleation, remaining vapors of silicon and metals co-condense on the nuclei. Silicide nanoparticles are then synthesized from the gas phase. The silicon content of the input feed powder is chosen to be 66.7 at.%, considered to be the stoichiometric composition of disilicides.

A. ITP flow model

The calculations used to derive the governing equations are based on the following assumptions: (i) steady-state laminar flow, (ii) axial symmetry, (iii) optically

thin, (iv) negligible viscous dissipation in energy equation, (v) negligible displacement current in comparison with the conductive current, (vi) negligible flow-induced electric field, (vii) heavy particles and electrons at identical temperature, and (viii) negligible effects of silicon and other metals on thermofluid fields or the plasma flow properties. Some researchers have reported that dense metal vapors affect the temperature field of a pure argon ICP in its higher temperature regions, especially when located near the induction coil because of its high electrical conductivity.[6,15,16] However, for the present operating conditions, the raw material is considered to be completely evaporated within the lower temperature region located below the injection tube. Metal vapors do not display high electrical conductivities at low temperature; consequently, the temperature field of the plasma flow is not significantly affected. Moreover, in the lower temperature region, where both nucleation and growth play important roles, the electrical conductivities of metal vapors are even lower. Therefore, effects due to the presence of metal vapor are neglected in this study. The laminar flow assumption is also justified because the Reynolds number is estimated to lie in the range 400–500 under the prevailing conditions.

The fields of flow, temperature, and concentration present in the induction thermal plasma flow were calculated by solving the two-dimensional continuity, momentum, energy, and species conservation equations, coupled with the use of Maxwell's equations. The non-equilibrium effects, introduced by the ionization and recombination, were also taken into account.

Continuity is represented by

$$\nabla \cdot (\rho u) = 0 \quad , \tag{1}$$

where ρ is the density and u is the velocity.

Momentum is represented by

$$\rho u \cdot \nabla u = -\nabla p + \nabla \tau + J \times B \quad , \tag{2}$$

where p is the pressure and τ is the viscous stress tensor. The last term on the right-hand side expresses the Lorentz force.

Energy is represented by

$$\rho u \cdot \nabla h = \nabla \cdot \left(\frac{\lambda}{C_p} \nabla h \right) - q_r + J \cdot E \quad , \tag{3}$$

where h is the enthalpy, λ is the thermal conductivity, C_p is the specific heart at constant pressure, and q_r is the radiation loss per unit volume. The last term expresses the Joule heating.

Species is represented by

$$\rho u \cdot \nabla Y = \nabla \cdot (\rho D \nabla Y) + R_r \quad , \tag{4}$$

where D is the diffusion coefficient, and R_r is the net production rate due to recombination and ionization. In

these equations, the conduction current J, the magnetic flux density B, and the electric field intensity E were obtained from Maxwell's equations.

The boundary conditions along the center line were set to ensure axial symmetry. At the wall of the plasma torch and the reaction chamber, non-slip conditions are maintained for the velocity, and the concentrations have zero gradient. The temperature present at the inside wall of the plasma torch was calculated, assuming that the outside wall was maintained at 300 K by water cooling. The injection tube was assumed to be at 500 K. The temperature at the wall of the reaction chamber was set to 300 K. The outflow boundary conditions were assumed that gradients of the variables are zero. The sheath gas has a swirl velocity component. Each gas stream has constant axial velocity, with zero radial velocity, and has a temperature of 300 K.

The EM field in the present study was analyzed on the basis of the two-dimensional modeling approach, with the electric field intensity functioning as the fundamental EM field variable.[17] Maxwell's equations are expressed in terms of the electric field intensity as follows

$$\nabla^2 E - \xi \sigma_e \frac{\partial E}{\partial t} = 0 \quad , \tag{5}$$

where ξ is the magnetic permeability and σ_e is the electrical conductivity. The associated boundary conditions for the EM fields are identical to those quoted in Ref. 17.

The transport properties of plasmas were obtained from the Chapman–Enskog method.[18] The radiation loss was estimated by the method described in Ref. 19. The net production rate can be obtained from the ionization rate constant and the recombination rate constant. In the present study, the ionization rate constant for argon was calculated from Eq. (6)[20]

$$k_{ion} = 3.75 \times 10^{-22} T^{1.5}(135300/T + 2) \exp$$
$$(-135300/T) \quad . \tag{6}$$

The recombination rate constant was calculated using the equilibrium constant.

The governing conservation equations were solved using Semi-Implicit Method for Pressure Linked Equation Revised (SIMPLER) algorithm.[21] The governing equations and the electric field intensity equation associated with the boundary conditions were discretized into finite differences, using the control-volume technique. Nonuniform grid points 30 × 30 were used for radial and axial directions, respectively. The grid was made finer close to the center and the coil region. Thermodynamic and transport properties were calculated from the temperature and compositions computed at each position in the calculation domain, at each iteration step.

J. Mater. Res., Vol. 20, No. 10, Oct 2005

2803

B. Multi-component co-condensation model

Vaporized metal and silicon are transported into the reaction chamber with the plasma gas, thereby decreasing its temperature. The temperature decrease causes the saturation pressure of the vapors to decrease, consequently the saturation pressure falls below the actual vapor pressure. This state of supersaturation leads to the production of nuclei by a nucleation mechanism (homogeneous nucleation). Simultaneously, metal vapors condense on the previously produced nuclei (heterogeneous condensation), the combined mechanisms leading to nanoparticle growth.[22] In the present study, a one-dimensional multi-component model is proposed to clarify the formation mechanism of silicide nanoparticles, involving the following assumptions: (i) spherical particles, (ii) negligible particle inertia due to their small size, (iii) velocity of the condensed phase is the same as that of the plasma gas, (iv) temperature of the nanoparticles is the same as that of the plasma gas, (v) negligible heat generation caused by condensation, (vi) metal and silicon vapors considered as ideal gases, (vii) negligible agglomeration among the nanoparticles, and (viii) atmospheric pressure maintained in the system. For the reaction chamber conditions, the information obtained by computation of the plasma flow is adopted and is modified for the one-dimensional model of the nanoparticle synthesis. In fact, a real flow has both an axial distribution and a radial distribution of its thermofluid fields. However, the thermofluid fields can be considered to be radially uniform when $r < 22.5$ mm under the inlet conditions of the reaction chamber. Moreover, axial convection predominates over radial diffusion for the mass-transfer of vapors. Therefore, a one-dimensional model can be reasonably applied under the present conditions.

The concentrations of the metal and silicon vapors present in the reaction chamber are obtained from the conservation equation, written as

$$\rho u \frac{\partial c_i}{\partial z} = -G_i \quad , \tag{7}$$

where c and G represent the mass fraction and the vapor consumption rate of the species i by nucleation and condensation, respectively.

Supersaturated vapors create nuclei by homogeneous nucleation. The homogeneous nucleation rate of the species i is taken as that proposed in Ref. 23.

$$I_i = \frac{(\beta_{11})_i n_{si}^2 S_i}{12} \sqrt{\frac{\Theta_i}{2\pi}} \exp\left(\Theta_i - \frac{4\Theta_i^3}{27(\ln S_i)^2}\right) \quad , \tag{8}$$

where S_i is the supersaturation ratio, defined as

$$S_i = \frac{n_{1i}}{n_{si}} = \frac{p_{1i}}{p_{si}} \quad , \tag{9}$$

and Θ is the normalized surface tension, written as

$$\Theta_i = \frac{\sigma_i s_{1i}}{k_B T} \quad , \tag{10}$$

where n, p, σ, s, and k_B are the number density, pressure, surface tension, surface area, and Boltzmann constant, respectively. Subscripts 1 and s denote the monomers and saturated states, respectively. When the Knudsen number Kn, which is the ratio of the mean free path to the particle diameter, is greater than 10, the collision frequency function for the free molecular regime between the a-mer and the b-mer β_{ab}, can be written as

$$\beta_{ab} = \left(\frac{3\upsilon_1}{4\pi}\right)^{1/6} \sqrt{\frac{6k_B T}{\rho}\left(\frac{1}{a} + \frac{1}{b}\right)} \, (a^{1/3} + b^{1/3})^2 \quad , \tag{11}$$

where υ is the volume, and a and b are equal to 1 for collisions occurring between molecules.

Since nuclei present in the low supersaturation state are unstable, due to their large growth rate and their corresponding large evaporation rate, nuclei are considered to be produced by homogeneous nucleation at higher supersaturations. These nuclei have the critical diameter, expressing their well-balanced condition of growth and evaporation. The critical diameter is written as

$$d_{pcr} = \frac{4\sigma_i \upsilon_{mi}}{k_B T \ln S_i} \quad , \tag{12}$$

where υ_m is the volume of the condensed molecule in the state of incipient melting.

In the state of high concentrations of nucleated particles and at low supersaturation, heterogeneous condensation becomes dominant and occurs on the surface of the nuclei, resulting in nanoparticle growth. The rate of nanoparticle growth by heterogeneous condensations, taking place among several species, can be estimated from the net molecular flux between the gas phase and the condensed phase, in considering all of the range of the Knudsen numbers[24]

$$\frac{d(d_{pi})}{dt} = \sum_j \frac{4\rho_g}{d_{pi}\rho_{cj}} D_j(X_{1j} - X_{sj}) \left\{\frac{1 + Kn_i}{1 + 1.7Kn_i + 1.333Kn_i^2}\right\} \quad , \tag{13}$$

where X is the molar fraction. The subscripts i and j represent the species of the vapors.

To determine the rate of homogeneous nucleation and subsequent nanoparticle growth by heterogeneous condensation, the temperature-dependent properties, such as the saturation pressure, density, and surface tension of the materials, were obtained from Ref. 25. Diffusion coefficients were estimated from the formula as proposed in Ref. 26.

A very fine computational grid is required for simulation of the nanoparticle synthesis since the nucleation and condensation processes have very much smaller characteristic times than that for the plasma flow. Thus, the grids for the reaction chamber (z = 190 to 380 mm) are divided into 5000 uniform grids in the z-direction for the nanoparticle synthesis. The data obtained from the computation performed on the plasma, such as temperature and velocity, are averaged radially in $r < 22.5$ mm and then modified axially for the finer grid system in order to calculate the rates of nucleation and condensation.

III. RESULTS AND DISCUSSION

Figures 2(a) and 2(b) show the temperature field and the flow field existing in the plasma torch, respectively. The Joule heating by the applied electromagnetic induction field generates the zone of remarkably high temperature (higher than 9500 K) in and immediately below the coil region. The high enthalpy of the plasma is subsequently transported to the downstream region by the convective flow. The radial temperature gradient is very steep near the torch wall since the wall is water-cooled. The characteristic recirculation flow exists above the coil region since the radial Lorentz force, induced in the plasma, pinches the flow.
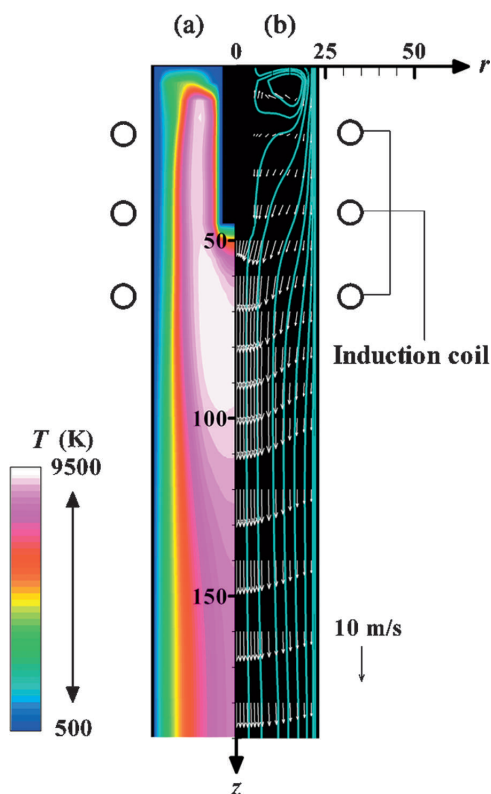
Figures 3(a) and 3(b) show the temperature field and the flow field in the reaction chamber, respectively. The high temperature of 8500 K at the inlet of the reaction chamber decreases very rapidly to values below 500 K. As a result, a very high quenching rate (10^4–10^5 K/s) is sustained, leading to near ideal conditions to support particle nucleation.

Figures 4(a)–4(d), 5(a)–5(d), and 6(a)–6(d) show the axial evolution of the vapor pressure, the vapor consumption rate, and the condensation ratio, respectively. The saturation vapor pressures of the metals and silicon decrease, in tandem with the temperature decrease in all systems as shown in Fig. 4. In the Cr–Si system, silicon vapor becomes supersaturated, and the pressure decreases very rapidly due to vapor consumption by the particle growth mechanism with homogeneous nucleation and heterogeneous condensation occurring earlier than the fall in the pressure of chromium vapor, as shown in Fig. 5(a). At the downstream position, the chromium vapor pressure reaches its saturation pressure and it then decreases by the mechanism of heterogeneous condensation on silicon particles. Since the condensation is more dominant than the homogeneous nucleation at low levels of supersaturation, the homogeneous nucleation of chromium is not observed. When chromium vapor condenses on silicon particles, the deposited chromium is considered to be very well-mixed in the liquid silicon particles during the particle growth phase since the prevailing temperature is greater than the silicon melting temperature and chromium-silicide nanoparticles are rapidly formed. Figure 6(a) additionally indicates that some 70% of silicon vapor is converted to particles in only 1 mm from the nucleation position and in the very short period
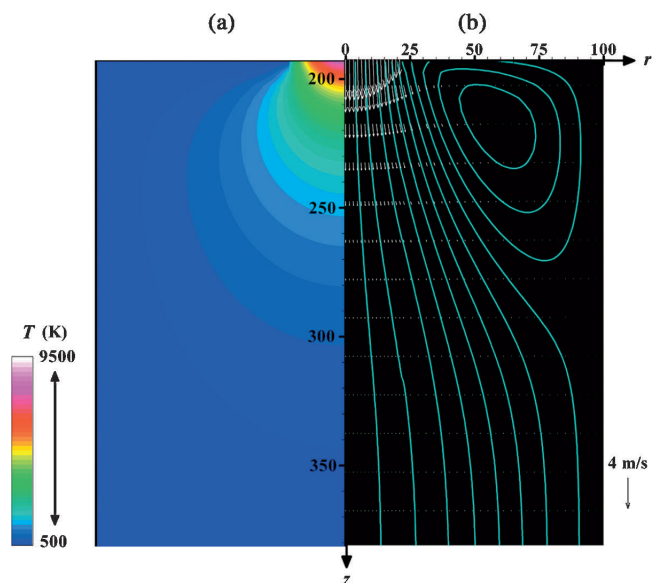

FIG. 2. Thermofluid fields in plasma torch: (a) temperature and (b) flow field.

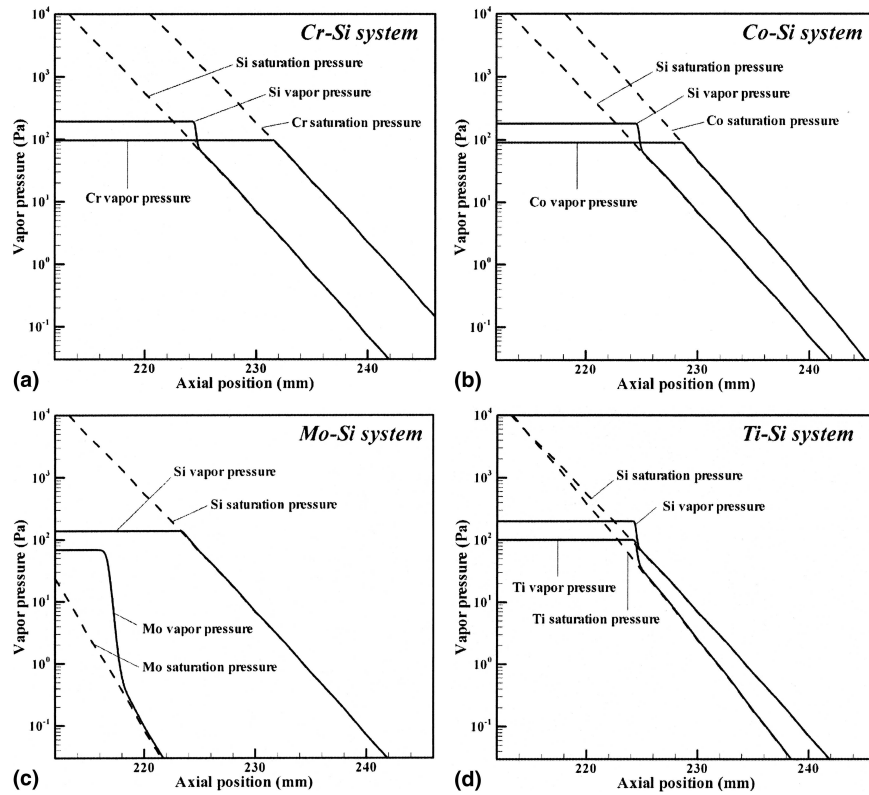FIG. 3. Thermofluid fields in reaction chamber: (a) temperature and (b) flow field.

FIG. 4. Axial evolution of vapor pressure for (a) Cr–Si system, (b) Co–Si system, (c) Mo–Si system, and (d) Ti–Si system.
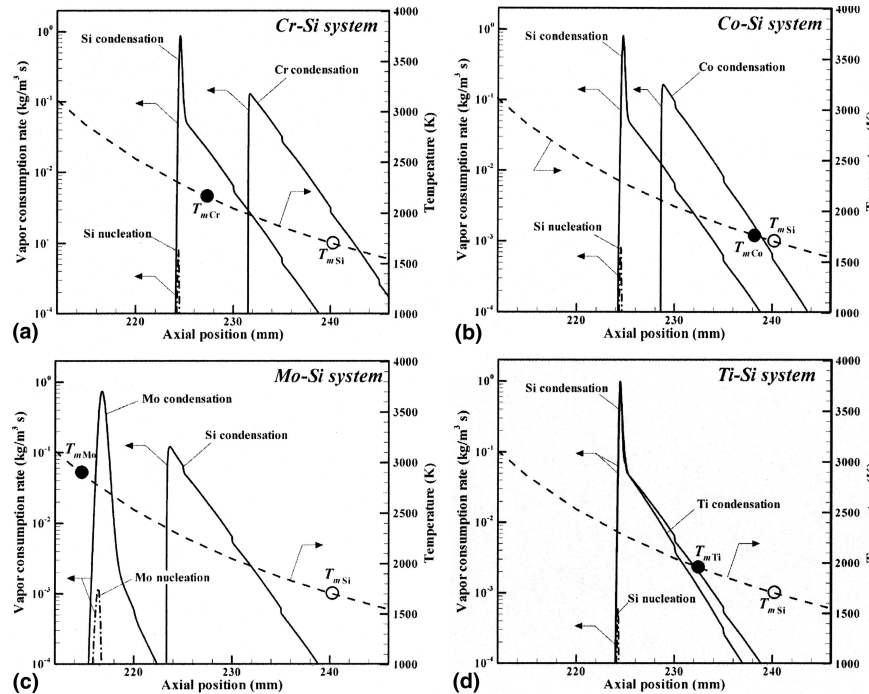

FIG. 5. Axial evolution of vapor consumption rate for (a) Cr–Si system, (b) Co–Si system, (c) Mo–Si system, and (d) Ti–Si system.

of 0.7 ms. Although the chromium vapor is converted at a more moderate pace than silicon vapor, the majority of the co-condensation process in the Cr–Si system is considered to be complete at the axial position of 242 mm. In

the Co–Si system, the same tendencies, as noted for the Cr–Si system, take place. The vapor pressure of cobalt decreases due to vapor consumption by the condensation process at a more upstream position compared to
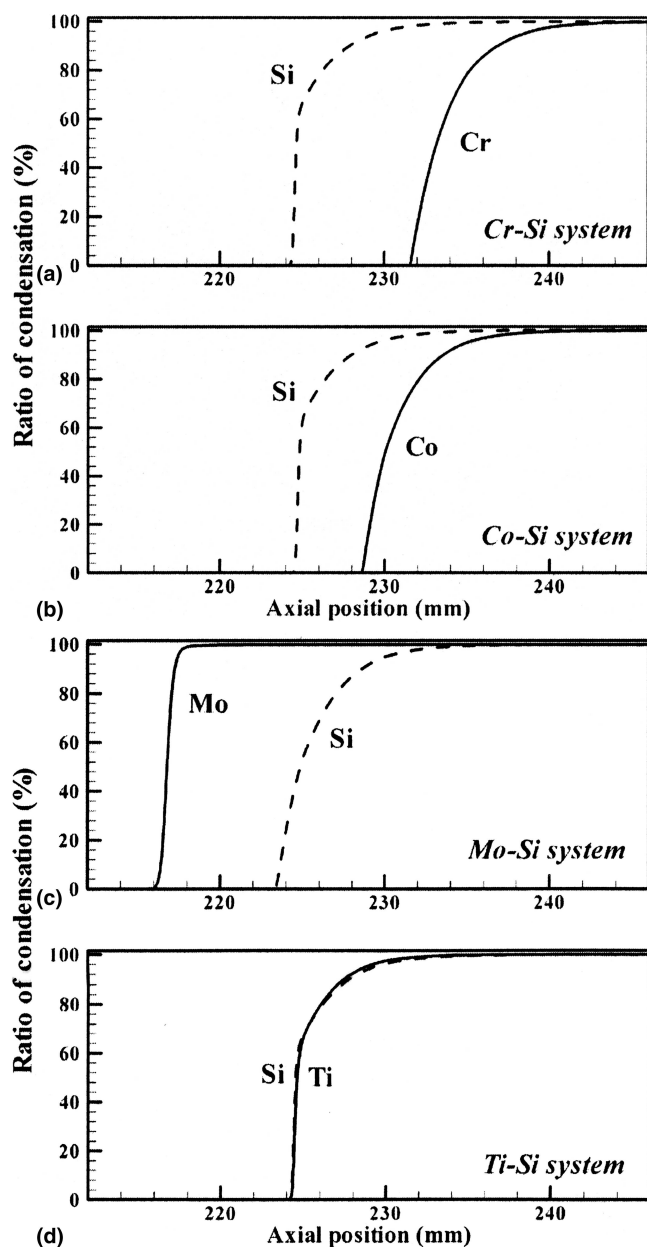
FIG. 6. Axial evolution of condensation ratio for (a) Cr–Si system, (b) Co–Si system, (c) Mo–Si system, and (d) Ti–Si system.

chromium in the Cr–Si system, as shown in Figs. 4(b), 5(b), and 6(b) since the saturation pressure of cobalt is lower than that of chromium. Thus, the condensation process in the Co–Si system is completed further upstream (239 mm), than is the case for the Cr–Si system as shown in Fig. 6(b).

In the Mo–Si system, molybdenum vapor becomes supersaturated and its concentration decreases rapidly at the more upstream position than that for silicon vapor since the saturation vapor pressure of molybdenum is much smaller than that of silicon, as shown in Fig. 4(c). Molybdenum particles grow by homogeneous nucleation and heterogeneous condensation; subsequently silicon

vapor condenses on the molybdenum particles without silicon nucleation, as shown in Fig. 5(c). Conversion of 99% of the initial molybdenum vapor into particles is completed in only 2 mm from the nucleation position, while the accompanying silicon vapor converts more slowly by condensation, as shown in Fig. 6(c). This figure also indicates that this co-condensation process finishes at the axial position of 234 mm.

In addition, Fig. 5(c) shows that the temperature of the nanoparticle growth region is lower than the melting point of molybdenum. This temperature gap leads to incomplete formation of silicides because molybdenum and silicon need to be well-mixed to form silicides during the growth step. However, the stoichiometric compounds of molybdenum-silicides were observed in the experiments.[11] These nanoparticles are, therefore, considered to grow in the super-cooled liquid state as a mixture of molybdenum and silicon, even at a temperature lower than the melting point of molybdenum because of the very high quenching rate achieved in the reaction chamber.

In the Ti–Si system, vapors of both titanium and silicon show small supersaturated states and decrease rapidly at the same axial position, as shown in Fig. 4(d). Figure 5(d) shows that silicon nucleates earlier than titanium. The vapors of silicon and titanium are consumed by heterogeneous condensation at the same time, after the nucleation of silicon. Titanium and silicon are considered to be well-mixed in the liquid state in this co-condensation process since the particles grow at temperatures higher than the melting points of titanium and silicon, resulting in further progress of the titanium-silicide formation. Eighty percent of both silicon and titanium vapors are converted to the condensed phase in only 2 mm from the silicon nucleation position, as shown in Fig. 6(d). The co-condensation process in this system is also eventually completed at the axial position of 234 mm.

Figures 7 (a)–7(d) show the final particle size distributions and silicon contents provided by the present model for the four silicon/metal systems. A number mean diameter in the particle size distribution is known to be equivalent to the first moment divided by the zeroth moment obtained from Moment-type approach.[22] However, as mentioned in Sec. I, the present method of calculation, with its high spatial resolution, is more effective in obtaining more accurate particle size distributions in the process where multi-component vapors are co-condensing in a very short time period. The number mean diameters obtained through the present calculations are 13.3 nm in the Cr–Si system, 12.8 nm in the Co–Si system, 8.5 nm in the Mo–Si system, and 15.8 nm in the Ti–Si system. The Mo–Si system produces smaller nanoparticles than those of other systems due to the difference in the nucleus size. Molybdenum nucleates with smaller
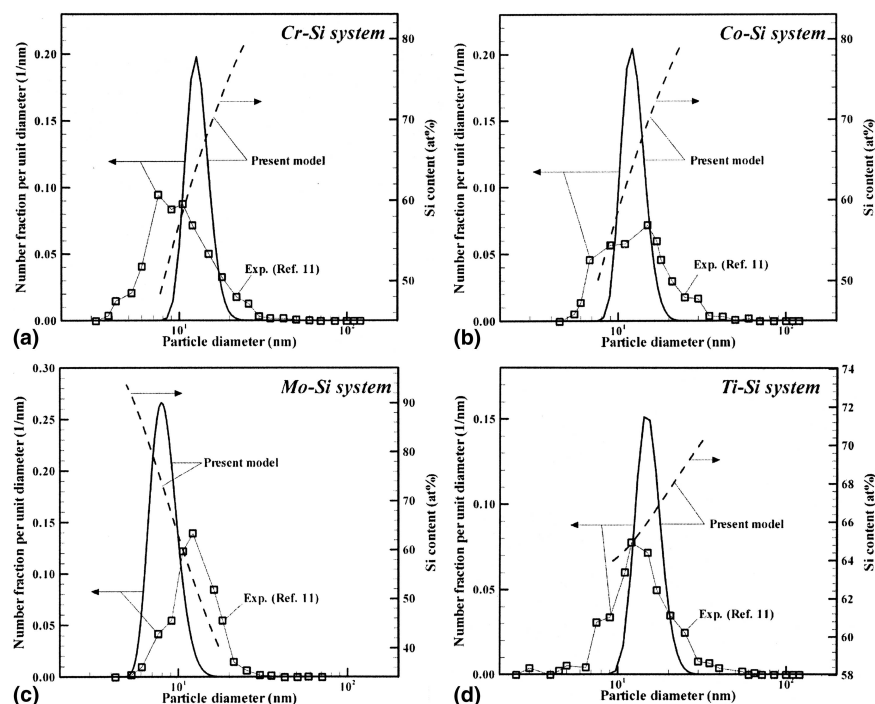
FIG. 7. Particle size distribution and silicon content for (a) Cr–Si system, (b) Co–Si system, (c) Mo–Si system, and (d) Ti–Si system.

critical diameters, from 0.59 to 1.94 nm, while the critical diameters of silicon nuclei present in other systems vary from 0.83 to 2.65 nm. Since a larger number of the smaller nuclei are produced in the Mo–Si system, a smaller quantity of the vapor is consumed per nucleus for particle growth. The Mo–Si system particle diameters are therefore smaller than those formed in other systems. In all systems, the particle size distributions agree well with the experimental results.[11] These show broader distributions than are estimated by the present modeling. This difference is attributed to agglomeration of the produced nanoparticles, as well as experimental errors arising from the instability of the plasma. Furthermore, turbulent dispersion of the nanoparticles might be operating, although the Reynolds number is estimated to be 400–500. The melting temperature change due to the small particle size might also affect the nanoparticle growth as well. In this present study, thermophoresis and Brownian motion were not taken into account because their effects were considered to be small enough to be neglected. As the next step forward, the present model should be improved by considering the effects of agglomeration, turbulent dispersion, melting temperature change, thermophoresis, and Brownian motion on the nanoparticle synthesis process.

The silicon contents show some ranges along with the particle diameters in Figs. 7(a)–(d). The Cr–Si and Co–Si systems have a range of 48.1–79.4 at.% and 49.5–79.3 at.%, respectively. The Mo–Si system in particular has the very wide range 40–94 at.%. Only the Ti–Si system has a

quite narrow range, 64–70 at.%; this results in the more homogeneous synthesis of the disilicide. These ranges are determined by the balance between the content of the formerly produced nuclei and that of the following condensing vapor. This indicates that silicide nanoparticles, synthesized in the induction thermal plasma can provide some diverse compositions. Although nanoparticle formation in the reaction chamber is a non-equilibrium process, due to the high quenching rates achieved, the compositions of the products can be roughly evaluated from the assayed silicon contents by comparing them with the phase diagrams for the metal-silicide;[27] they are summarized in Table II. In all of the systems, the required disilicides (MSi_2) are successfully synthesized as the main products, while sub-products are also synthesized, even though the raw material powders are supplied with the disilicide stoichiometric compositions. This is because the condensation positions are different due to the different vapor pressures of the input materials. In the experiment,[11] Cr_5Si_3 and Ti_5Si_3 were observed in their systems although they are not indicated from present

TABLE II. Compositions of synthesized silicide nanoparticles estimated from phase diagrams (Ref. 24).

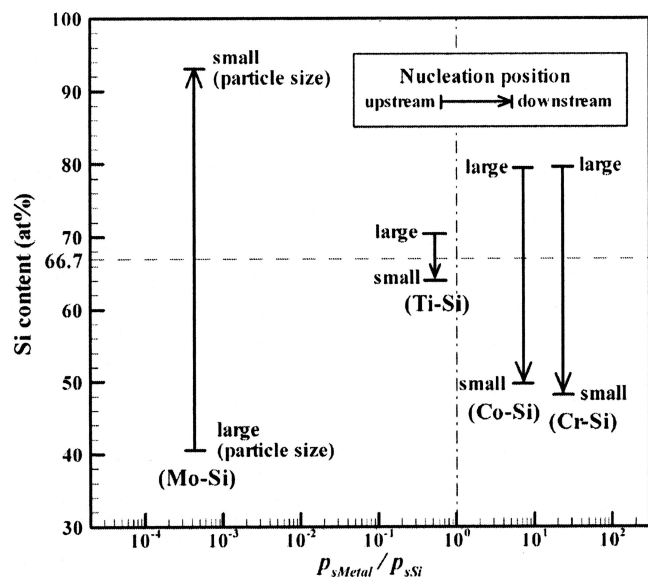| System	Main product	Sub-product
Cr–Si	$CrSi_2$	Cr_5, Si_3, $CrSi$, Si
Co–Si	$CoSi_2$	$CoSi$, Si
Mo–Si	$MoSi_2$	Mo_5Si_3, Si
Ti–Si	$TiSi_2$	$TiSi$, Si

FIG. 8. Correlation chart between saturation pressure ratio and silicon content.

model predictions. The initial average diameters of the feed powders for chromium and titanium were reported to be relatively larger (Cr: 9.6 μm, Ti: 9.1 μm) than those of cobalt and molybdenum (Co: 5.0 μm, Mo: 3.0 μm). Thus, powders of chromium or titanium did not evaporate instantaneously but continued to evaporate in the downstream region. Consequently, some silicides were considered to be prepared in a metal-rich state in the Cr–Si and Ti–Si systems. However, most of the results for compositions of the synthesized silicide nanoparticles also show good agreement with experiment.[11] This indicates that the present model adequately describes the phenomena occurring in silicide nanoparticle synthesis using induction thermal plasmas under atmospheric pressure, although there is some room for improvement.

Figure 8 shows the correlation chart between the saturation pressure ratios and the silicon contents at the nucleation positions, obtained from the present study. Larger particles, with their silicon nuclei generated upstream, provide for larger silicon contents in the Cr–Si, Co–Si, and Ti–Si systems, while smaller particles, with their molybdenum nuclei generated downstream, provide for larger silicon contents as formed in the Mo–Si system. Furthermore, the silicon contents are scattered when condensations of metal and silicon occur at different axial positions due to the largely different characteristic vapor pressures as shown in the Cr–Si, Co–Si, and Mo–Si. The silicon content shows a particularly narrow composition range when condensation of metal and silicon occur simultaneously, as shown in the Ti–Si system.

Figure 8 thus indicates that systems with large differences of saturation pressures between the metal and the silicon tend to produce silicide nanoparticles with a wide range of compositions. Nanoparticle synthesis, including co-condensation processes, should be considered and discussed primarily with respect to nucleation temperature. However, this parameter is usually difficult to estimate. It is, therefore, more expedient to evaluate the composition of the nanoparticles from the viewpoint of the saturation pressures of the metal and silicon. This chart can be used conveniently for the prediction of nanoparticle composition in the co-condensation process, on the basis of the saturation pressure ratio.

IV. CONCLUSIONS

Numerical analysis has been conducted to clarify the formation mechanisms of silicide nanoparticles produced in an induction thermal plasma operation at atmospheric pressure. The thermofluid fields in an induction thermal plasma were determined using an electromagnetic fluid dynamics approach, and a multi-component co-condensation model has been proposed to describe the formation taking place during the silicide nanoparticle synthesis.

(1) The remarkably high temperature zone (higher than 9,500 K) is generated by Joule heating within the plasma torch, and the high quenching rate (10^4–10^5 K/s) is obtained subsequently in the reaction chamber.

(2) In the Cr–Si system and the Co–Si system, silicon vapor is consumed by particle growth with homogeneous nucleation and heterogeneous condensation, subsequently metal vapor heterogeneously condenses on the liquid silicon particles. The Mo–Si system shows an opposite tendency to those systems. In the Ti–Si system, vapors of silicon and titanium are simultaneously consumed by heterogeneous condensation on silicon nuclei. In all systems, the co-condensation processes complete in a very short period.

(3) Each system produces nanoparticle diameters of around 10 nm and provides the required disilicide with the stoichiometric composition. The Mo–Si system produces smaller nanoparticles than the other systems due to the larger number of smaller nuclei. The Cr–Si, Co–Si, and Mo–Si systems generate particles of wide ranges of silicon content, while only the Ti–Si system generates a narrower composition range, indicating the more homogeneous synthesis of the disilicide.

(4) The correlation chart between the saturation pressure ratio and the silicon content is also presented. The composition of the nanoparticles can be evaluated from the saturation pressure ratio between the metal and silicon. Processes including large differences in the saturation pressures tend to produce diverse silicide nanoparticles. This correlation chart can be used for the prediction of nanoparticle compositions formed in the co-condensation process.

The present study indicates that induction thermal plasmas, with their high enthalpies and high quenching

rates are very effective, even for the more difficult co-condensation processes where large vapor pressure differences exist. The present model should be improved by considering the effects of agglomeration, turbulent dispersion, melting point change, thermophoresis, and Brownian motion, on the nanoparticle synthesis, as matters prepared to receive attention in our future work.

ACKNOWLEDGMENT

NOTATION

B	magnetic flux density (T)
c	mass fraction of condensing vapor
C_p	specific heat at constant pressure (J/kg K)
D	diffusion coefficient (m^2/s)
d_p	particle diameter (m)
E	electric field intensity (V/m)
G	vapor consumption rate (kg/m^3 s)
h	enthalpy (J/kg)
I	homogeneous nucleation rate (l/m^3 s)
J	conduction current (A/m^2)
Kn	Knudsen number
k_B	Boltzmann constant (J/K)
k_{ion}	ionization coefficient (m^3/s)
M	metal
m	mass (kg)
n	number density (l/m^3)
p	pressure (Pa)
Q	flow rate (Sl/min)
q_r	radiation loss (W/m^3)
r	radial coordinate (m)
s	surface (m^2)
S	supersaturation ratio
T	temperature (K)
t	time (s)
u	velocity (m/s)
u	velocity component in axial direction (m/s)
υ	volume (m^3)
X	molar fraction
Y	mass fraction
z	axial coordinate (m)
β	collision frequency function (m^3/s)
ξ	magnetic permeability (H/m)
Θ	normalized surface tension
λ	thermal conductivity (W/m K)
ρ	density (kg/m^3)
σ	surface tension (N/m)
σ_e	electrical conductivity (S/m)

Subscripts

C	coil
Co	cobalt
Cr	chromium
c	condensed phase
cr	critical
g	gas phase
Mo	molybdenum
m	melting
Si	silicon
s	saturation
Ti	titanium
W	wall
l	monomer

REFERENCES

1. M. Sakano, T. Watanabe, and M. Tanaka: Numerical and experimental comparison of induction thermal plasma characteristics between 0.5 MHz and 4 MHz. *J. Chem. Eng. Jpn.* **32,** 619 (1999).
2. M. Sakano, M. Tanaka, and T. Watanabe: Application of radio-frequency thermal plasmas to recover materials from fly ash. *Thin Solid Films* **386,** 189 (2001).
3. M. Shigeta, T. Sato, and H. Nishiyama: Numerical simulation of a potassium-seeded turbulent RF inductively coupled plasma with particles. *Thin Solid Films* **435,** 5 (2003).
4. M. Shigeta, T. Sato, and H. Nishiyama: Computational experiment of a particle-laden RF inductively coupled plasma with seeded potassium vapor. *Int. J. Heat Mass Transfer* **47,** 707 (2004).
5. Japan Society of Mechanical Engineers: *Functional Fluids and Intelligent Fluids* (Corona Pub. Corp., Japan, 2000), p. 2.
6. H. Nishiyama and M. Shigeta: Numerical simulation of an RF inductively coupled plasma for functional enhancement by seeding vaporized alkali metal. *European Phys. J., Appl. Phys.* **18**(2), 125 (2002).
7. S.L. Girshick, C-P. Chiu, R. Muno, C.Y. Wu, L. Yang, S.K. Singh, and P.H. McMurry: Thermal plasma synthesis of ultrafine iron particles. *J. Aerosol Sci.* **24**(3), 367 (1993).
8. T. Watanabe and K. Fujiwara: Control of diameter and yield of silicon dioxide ultrafine particles prepared by radio frequency thermal plasmas. *J. Soc. of Inorg. Mater. Jpn.* **7,** 285 (2000).
9. M. Shigeta, T. Watanabe, and H. Nishiyama: Numerical investigation for nanoparticle synthesis in an RF inductively coupled plasma. *Thin Solid Films* **457,** 192 (2004).
10. T. Watanabe, A. Nezu, Y. Abe, Y. Ishii, and K. Adachi: Formation mechanism of electrically conductive nanoparticles by induction thermal plasmas. *Thin Solid Film* **435,** 27 (2003).
11. T. Watanabe and H. Okumiya: Formation mechanism of silicide nanoparticles by induction thermal plasmas. *Sci. and Technol. Advanced Mater.* **5,** 639 (2004).
12. J. Mostaghimi, P. Proulx, and M.I. Boulos: An analysis of the computer modeling of the flow and temperature fields in an inductively coupled plasma. *Numerical Heat Trans.* **8,** 187 (1985).
13. J-F. Bilodeau and P. Proulx: A mathematical model for ultrafine iron powder growth in thermal plasma. *Aerosol Sci. Tech.* **24,** 175 (1996).
14. M. Desilets, J-F. Bilodeau, and P. Proulx: Modelling of the reactive synthesis of ultra-fine powders in a thermal plasma reactor. *J. Phys. D: Appl. Phys.* **30,** 1951 (1997).

2810

J. Mater. Res., Vol. 20, No. 10, Oct 2005

15. K.C. Paul, T. Takashima, and T. Sakuta: Copper vapor effect on RF inductively coupled SF_6 plasmas. *IEEE Trans. Plasma Sci.* **26,** 1000 (1998).

16. C. Wang, T. Imahori, Y. Tanaka, T. Sakuta, H. Takikawa, and H. Matsuo: Silicon inclusion effect on fullerene formation under induction thermal plasma condition. *Thin Solid Films* **407,** 72 (2002).

17. X. Chen and L. Pfender: Modeling of RF plasma torches with a metallic tube inserted for reactant injection. *Plasma Chem. Plasma Proc.* **11,** 103 (1991).

18. J.O. Hirschfelder, C.F. Curtiss, and R.B. Bird: *Molecular Theory of Gases and Liquids* (John Wiley, New York, 1964), p. 484.

19. R.C. Miller and R.I. Ayen: Temperature profiles and energy balance for an inductively coupled plasma torch. *J. Applied Phys.* **10,** 5260 (1969).

20. M.I. Hoffert and H. Lien: Quasi-one-dimensional, nonequilibrium gas dynamics of partially ionized two-temperature argon. *Phys. Fluids* **10,** 1769 (1967).

21. S.V. Patankar: *Numerical Fluid Dow and Heat Transfer* (Hemisphere, New York, 1980), p. 138.

22. S.K. Friedlander: *Smoke, Dust and Haze, Fundamentals of Aerosol Dynamics,* 2nd ed. (Oxford Univ. Press, Oxford, U.K., 2000) p. 275.

23. S.I. Girshick, C.P. Chiu, and P.H. McMurry: Time-dependent aerosol models and homogeneous nucleation rates. *Aerosol Sci. Technol.* **13,** 465 (1990).

24. S.V. Joshi, Q. Liang, J.Y. Park, and J.A. Batdorf: Effect of quenching conditions on particle formation and growth in thermal plasma synthesis of fine powders. *Plasma Chem. Plasma Proc.* **10,** 339 (1990).

25. Japan Institute of Metals: *Metal Data Book* (Maruzen, Japan, 1993), p. 16.

26. G.M. Phanse and S.E. Pratsinis: Theory for aerosol generation in laminar flow condensers, *Aerosol Sci. Technol.* **11,** 100 (1989).

27. T.B. Massalski: *Binary Alloy Phase Diagrams,* 2nd ed. 3 (American Society for Metals, Materials Park, 1990), p. 2664.